PHYSICAL REVIEW B VOLUME 26, NUMBER 6 15 SEPTEMBER 1982

k-resolved inverse photoelectron spectroscopy and its application to Cu(001), Ni(001), and Ni(110)

D. P. Woodruff,* N. V. Smith, P. D. Johnson, and W. A. Royer
Bell Laboratories, Murray Hill, New Jersey 07974
(Received 2 April 1982)

Experimental results on Cu(001), Ni(001), and Ni(110) with the use of the newly developed technique of k-resolved inverse photoelectron spectroscopy (or angle-resolved ultraviolet bremsstrahlung isochromat spectroscopy) are presented and compared with the predictions of bulk band-structure theory. A theoretical model is obtained by inverting the well-known three-step model for ordinary photoemission taking the optical transitions to be direct. Detailed band calculations are performed with full inclusion of momentum matrix elements using a combined interpolation scheme. A two-band approximation is also propounded and is found to be adequate in some circumstances. Results obtained on Cu(001) and Ni(001) for the $E(\vec{k}_{\|})$ energy dispersion relations of peaks in the spectra at the photon energy $\hbar\omega = 9.7$ eV are shown to be in excellent agreement with bulk band theory. The variation in peak intensity with parallel wave vector $k_{\|}$ shows agreement with calculated momentum matrix elements. For Ni(001), the relative intensities of transitions into the s,p bands and into the unoccupied minority-spin d bands are qualitatively understood in terms of direct transitions. In the case of normal incidence ($k_{\|}=0$) on Ni(110), it appears that bulk direct transitions are insufficient to explain the data, and it is necessary to invoke density-of-states contributions. Some speculations on future directions are advanced.

I. INTRODUCTION

Bremsstrahlung isochromat spectroscopy[1] is essentially the inverse of photoelectron spectroscopy (PES).[2,3] The technique consists of bombarding a sample with electrons of energy E, some of which penetrate into the bulk and then decay radiatively. Spectra are obtained by sweeping E and monitoring the emergent photon flux at some fixed photon energy $\hbar\omega$. It is thereby possible to map out features of the unoccupied density of states. An important advantage of this *inverse* photoelectron spectroscopy (IPES) is that it permits investigation of electronic states between the Fermi level and the vacuum level, a range inaccessible in ordinary PES.

In this paper we report the results of experiments and theoretical calculations intended to explore the possibilities of *k-resolved* inverse photoemission spectroscopy (KRIPES). The incoming electron beam is incident upon a single-crystal surface along a well-defined direction. Thus the wave vector $\vec{k}$ of the incident electron is specified in a manner analogous to the angle-resolved mode of PES. We show that KRIPES is quite feasible.[4] Our principal new result is the observation of energy dispersion of peaks in the KRIPES data, very reminiscent of that seen in angle-resolved PES. We show furthermore that the dispersion and much of the intensity behavior, can be understood in terms of direct transitions within the bulk band structure.

The format of this paper is as follows. In Sec. II we advance a simple theoretical model for KRIPES. It is basically a straightforward inversion of the well-known three-step model for PES[5] We also present the two-band approximation which is of particular pedagogical value in understanding the energy dispersion results. Considerable qualitative discussion is devoted to those physical features omitted by the simple three-step model based on bulk direct transitions. Section III describes our experimental methods, with particular emphasis on those things done differently from previous IPES work. Results on Cu(001), Ni(001), angle-integrated Ni, and Ni(110) are presented in Sec. IV and are interpreted (as far as possible) in terms of the inverted three-step model of Sec. II. Finally, in Sec. V we express some thoughts on promising future directions for KRIPES.

II. THEORY

A. Inverting the three-step model

A formal theory of inverse photoemission has been propounded by Pendry[3] very much in the spirit of the one-step models of photoemission.[6] If we appeal to the history of PES, however, it is well known that the more formal one-step theories were preceded by a much simpler three-step model which had proved itself to be very successful in many cases.[7] In the three-step model the photoemission process is separated into the following three parts, each of which is treated by some simple model: (1) *optical excitation* in the interior of the sample; (2) *transport* to the surface without suffering energy loss through electron-electron scattering; (3) *escape* across the surface. Inversion of this model appropriate to bremsstrahlung emission leads to the following analogous three steps and associated parametrization.

Step 1. Penetration of the system. The incoming electron couples into one of the unoccupied states of the bulk solid. The coupling probability, which we shall call c_i, will be discussed later.

Step 2. Competition between nonradiative and radiative decay. After penetration into the solid there is a strong probability $\beta(E)$ that the electron will decay nonradiatively through inelastic electron-electron scattering. This is the physical origin of the very short values ($l \lesssim 10-20$ Å) for the penetration depths of low-energy electrons. The remaining fraction, $1-\beta(E)$, decay radiatively giving rise to the measured bremsstrahlung. The photon attenuation lengths are much greater than l, so photon attenuation should not constitute an obstacle to emission of the bremsstrahlung. We shall assume that the factor $(1-\beta)$ is sufficiently slowly varying over the energy range of interest here that we will need not take it into account in these, our first attempts to interpret KRIPES data. (See further discussion in Sec. II E.)

Step 3. Optical deexcitation. It is assumed that the radiative decay takes place by means of a direct (i.e., $\vec{k}$-conserving) transition within the bulk band structure. The electron occupies a state at $\vec{k}$ in the Brillouin zone at initial energy $E_i(\vec{k})$ and decays vertically to a final energy $E_f(\vec{k})$. This assumption of direct transitions is the most fundamental ingredient of our present discussion, and constitutes the basis of most of our interpretation in Sec. IV.

By analogy with photoemission, the bremsstrahlung photon flux at $\hbar\omega$ for incident electrons of energy E may be written

$$N(\hbar\omega,E) \propto \sum_{f,i} \int_{\Omega} d^3k \, |P_{fi}|^2 c_i \times \delta(E_i(\vec{k})-E_f(\vec{k})-\hbar\omega) \times \delta(E-E_i(\vec{k})) \, . \quad (1)$$

$|P_{fi}|^2$ is the square of the momentum matrix element and f and i are band indices; it is understood, of course, that both initial and final states are unoccupied. The volume of integration Ω over $\vec{k}$ space is determined by experimental conditions. For example, for normal incidence of the electrons Ω would be a narrow rod passing through the origin and parallel to the surface normal. At the other extreme, for experiments which are thoroughly angle integrated, Ω would encompass the entire Brillouin zone.

B. Band-structure computations

We have performed numerical calculations of the band energies $E_i(\vec{k})$ and $E_f(\vec{k})$, the momentum matrix elements $|P_{fi}|$, and the integral of Eq. (1) using a combined interpolation scheme.[8] The essential features of the results are illustrated here for the case of Cu(001). We limit our discussion to $\hbar\omega=9.7$ eV, the photon energy used in our experiments.

For the case of normal incidence of the electrons on Cu(001), the parallel component of the electron wave vector vanishes ($\vec{k}_{||}=0$), and so we are confined to that part of the band structure along the ΓX direction illustrated in Fig. 1(a). At $\hbar\omega=9.7$ eV there is only one possible vertical transition in the energy range shown, and it deposits an electron at the energy $E_f=0.4$ eV relative to the Fermi level.

Away from normal incidence, we have

$$k_{||}=[2m(E-E_v)/\hbar^{-2}]^{1/2}\sin\theta \, , \quad (2)$$

where θ is the angle of electron incidence and E_v is the vacuum level. To find the corresponding values of E_f, the computation consists of hunting for the isochromat surface given by

$$E_i(\vec{k})-E_f(\vec{k})-\hbar\omega=0 \, , \quad (3)$$

where $\hbar\omega=9.7$ eV. The nature of the hunt is illustrated in Figs. 1(b) and 1(c) which show the band structure of Cu along lines parallel to ΓX for two different values of $k_{||}$. There are two main changes affecting KRIPES: First, the final energy

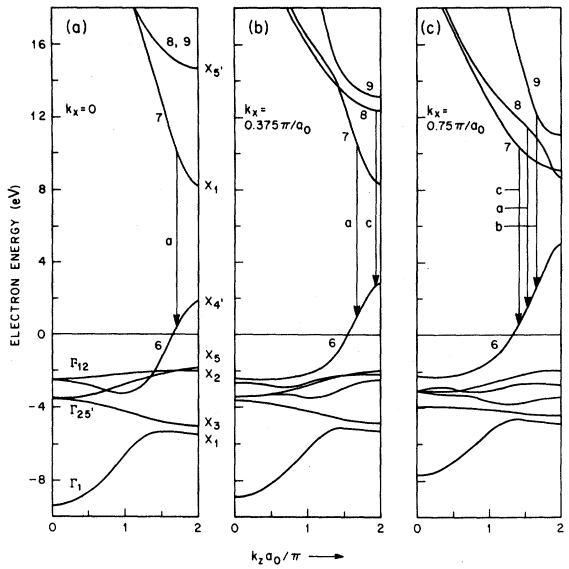

FIG. 1. Band structure of Cu: (a) Along the ΓX direction, appropriate to normal incidence KRIPES on the Cu(001) surface; (b) and (c) along directions parallel to ΓX with $k_{\parallel}=0.375(\pi/a_0)$ and $0.75(\pi/a_0)$, respectively. The vertical arrows indicate the direct transitions for $\hbar\omega=9.7$ eV. a_0 is the bulk-lattice parameter ($=3.615$ Å for Cu).

E_f for the $\hbar\omega=9.7$ eV direct transition initially increases with $k_{\parallel}$; second, the double degeneracy between bands 8 and 9 is lifted and these bands move to lower energies, eventually becoming available as initial-state bands for additional direct transitions at $\hbar\omega=9.7$ eV. This is all summarized in Fig. 2 which displays the isochromat curves and the $E_f(\vec{k}_{\parallel})$ dispersion curves for the two principal symmetry directions in the Cu(001) surface. There are a number of different sheets of the isochromat surface since several band pairs (i,f) can contribute in this energy range. The final state is always in band 6 ($f=6$), but the initial-state band can range over $i=7$, 8, and 9.

Band-structure calculations employing the combined interpolation scheme are also able to generate values for the momentum matrix elements (or optical strength) of the direct transitions. For Bloch wave functions, the momentum operator is given by the derivative relationship

$$\vec{P}=\frac{m}{\hbar}\frac{\partial H(\vec{k})}{\partial \vec{k}}\ , \tag{4}$$

where $H(\vec{k})$ is the parametrized Hamiltonian of the scheme.

Useful approximations can also be generated for the coupling coefficients c_i. For example, in the case of electron incidence on Cu(001), coupling is expected to be most efficient when the wave function of the initial state $E_i(\vec{k})$ contains a large admixture of the plane wave $\exp[i(\vec{k}+\vec{G})\cdot\vec{r}]$ where $\vec{G}$ is the (0,0,−2) reciprocal-lattice vector. The parallel component $\vec{k}_{\parallel}+\vec{G}_{\parallel}$ of this wave is relatively small, permitting good matching to incoming external waves. We shall explore the consequences of this kind of approximation in more detail in Sec. IV.

C. Two-band approximation

Since we are concerned only with unoccupied states, the d bands of Cu do not really enter the problem. The transitions occur only between the free-electron-like bands. A simple and physically transparent approximation here is the two-band model based on the two-plane waves $\exp(i\vec{k}\cdot\vec{r})$ and $\exp[i(\vec{k}+\vec{G})\cdot\vec{r}]$ where $\vec{G}$ is an appropriate reciprocal-lattice vector. For the case of Cu(001)

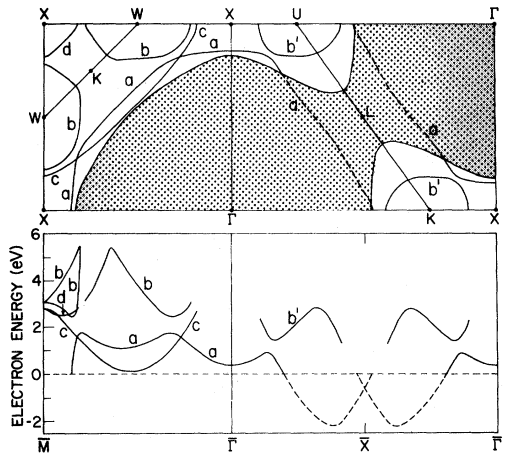

FIG. 2. Theoretical isochromat curves at $\hbar\omega=9.7$ eV for the two principal symmetry directions in the Cu(001) surface. Upper part: The vertical ΓX line corresponds to $\vec{k}_{\parallel}=0$; the shaded area corresponds to the occupied region within the Fermi surface; curves labeled a, b, b', c, and d correspond to surfaces of constant interband energy difference ($\hbar\omega=9.7$ eV) between bands 7, 8, 9, and band 6; the notation Γ, X, W, K, U, L refers to the conventional three-dimensional Brillouin zone. Lower part: The final energies E_f are plotted as a function of $\vec{k}_{\parallel}$ for the various branches a, b, b', c, and d; the notation $\bar{\Gamma},\bar{M},\bar{X}$ refers to the two-dimenstional surface Brillouin zone.

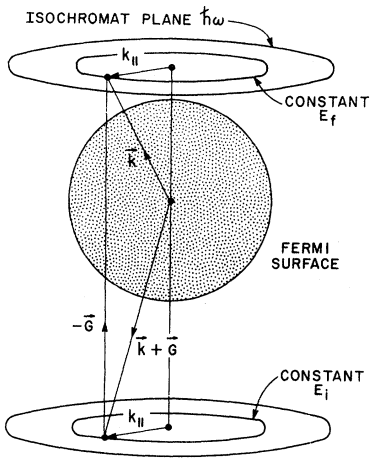

FIG. 3. Geometry of the two-band approximation appropriate to inverse photoemission. An electron of energy E_i emits a photon of energy $\hbar\omega$ and simultaneously executes an umklapp process through reciprocal-lattice vector $-\vec{G}$.

depicted in Fig. 1, we would take $\vec{G}$ as the (0,0−2) reciprocal-lattice vector. The two-band model has been considered in the case of ordinary PES by a number of authors.[9,10] We reexpound the model here for the case of inverse photoemission. The model is helpful in illuminating the essential features of the more exact band-structure model. It is also adequate in predicting the experimentally measured $E_f(\vec{k}_{\parallel})$ dispersion curves.

Let V_G represent the pseudopotential coefficient through which the two-plane waves interact. Writing $E_{\vec{k}}=\hbar^2k^2/2m$ and $E_{\vec{k}+\vec{G}}=\hbar^2(\vec{k}+\vec{G})^2/2m$, we have

$$2E_i(\vec{k})=(E_{\vec{k}+\vec{G}}+E_{\vec{k}})+[(E_{\vec{k}+\vec{G}}-E_{\vec{k}})^2+4V_G^2]^{1/2}, \quad (5)$$

$$2E_f(\vec{k})=(E_{\vec{k}+\vec{G}}+E_{\vec{k}})-[(E_{\vec{k}+\vec{G}}-E_{\vec{k}})^2+4V_G^2]^{1/2}. \quad (6)$$

The isochromat surface of Eq. (3) is then given by the following plane in $\vec{k}$ space:

$$(\hbar^2/m)\vec{k}\cdot\vec{G}=[(\hbar\omega)^2-4V_G^2]^{1/2}-E_G, \quad (7)$$

where $E_G\equiv\hbar^2G^2/2m$. From cylindrical symmetry about the direction of $\vec{G}$, the contours of constant E_f or E_i are circles on the isochromat plane. This is illustrated in Fig. 3. In terms of the parallel component $\vec{k}_{\parallel}$, i.e., the component of $\vec{k}$ in the isochromat plane (and therefore perpendicular to $\vec{G}$), we have

$$E_i(\vec{k}_{\parallel})=\hbar^2k_{\parallel}^2/2m+[(E_G+\hbar\omega)^2-4V_G^2]/4E_G, \quad (8)$$

$$E_f(\vec{k}_{\parallel})=\hbar^2k_{\parallel}^2/2m+[(E_G-\hbar\omega)^2-4V_G^2]/4E_G. \quad (9)$$

The dispersion in this approximation is therefore perfectly free-electron-like in $k_{\parallel}$, plus some constant energy. For constant E_i or E_f the electron states are distributed around a cone[10] with its axis along the direction of $\vec{G}$.

Features of the two-band approximation are readily recognizable in the more elaborate band-structure results of Fig. 2. The prediction of the two-band model that the isochromat surface should be a plane can be seen in vestigial form in the result that the isochromat curves of Fig. 2 frequently run closely parallel to zone boundaries. Crossings between such curves are removed by the mutual pseudopotential interactions between bands 7, 8, and 9. As a principal example, note that close to $\vec{k}_{\parallel}=0$ the isochromat curve for branch a runs parallel to the zone-boundary line $XWXU\Gamma$. At higher values of $k_{\parallel}$, the character of the two-band model jumps the gaps and follows branches b or b' which also run more or less parallel to $XWXU\Gamma$. In the lower part of Fig. 2 it is seen that the corresponding branches of the $E_f(\vec{k}_{\parallel})$ dispersion curve adhere closely to a free-electron-like parabola in accordance with Eq. (9).

In the two-band approximation the momentum matrix elements are given by

$$\vec{P}_{fi}=\vec{G}(V_G/\omega), \quad (10)$$

and are therefore independent of E_i, E_f, and $\vec{k}$ insofar as V_G is independent of these quantities. This is in distinct contrast to the more complete band-structure results, as will be discussed in Secs. IV A and IV B.

D. Density-of-states and surface effects

Appealing once again to the history of ordinary PES, it was established eventually that the bulk band-structure approach is incomplete. Additional features in PES are explained variously as density-of-states effects, band-gap emission, or surface states and/or resonances.[7,11] We expect similar departures in IPES and KRIPES.

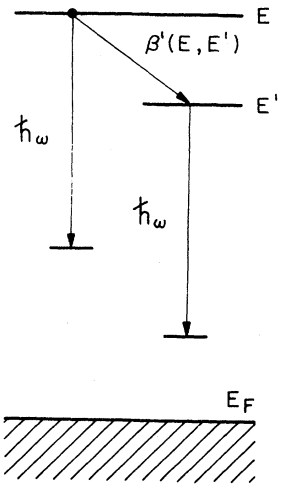

FIG. 4. Origin of the inelastic background in IPES. An incoming electron of energy E may directly decay radiatively yielding a photon $\hbar\omega$. Photons of energy $\hbar\omega$ may also be generated after a nonradiative inelastic decay to energy E'.

For single-crystal surfaces, translational periodicity guarantees that $\vec{k}_{||}$ is a good quantum number. The existence of the surface and the shortness of the electron-penetration depth imply that $k_\perp$ is no longer a good quantum number and therefore need not be completely conserved in the optical-deexcitation transition. Relaxation of $k_\perp$ conservation leads us to expect KRIPES data to reflect strong features in the one-dimensional density of states (1D DOS) corresponding to the prescription for determining $\vec{k}_{||}$ from the experimental conditions. For example, in normal incidence KRIPES we sample the one 1D DOS along the line defined by the equation $\vec{k}_{||}=0$. In the case of IPES (angle-integrated data) we would expect the relaxation of $\vec{k}_\perp$ conservation to lead to spectra displaying features characteristic of the total density of states (DOS).

In the presence of a surface, the initial-state wave function is not simply a Bloch function but contains also functions of evanescent character. For example, even when the incoming electron encounters an absolute energy gap of the bulk solid, it can still couple into the system through these evanescent functions. (See the phenomenon of "band-gap emission" in ordinary PES.) Finally, there exist surface states and surface resonances which can in principle contribute features to IPES and KRIPES data. In the case of Ni(110), for example, we shall in Sec. IV D be led to consider DOS effects. For the most part, however, we find that a bulk band-structure approach is adequate to interpret our present data, just as in the early days of PES.

E. Other omissions

The theoretical predictions generated by the model described here are of course, far from complete. We have mentioned already our neglect of the factor $1-\beta$, where β is the probability of nonradiative decay of the incoming electron. A related problem is the existence of an inelastic background to the spectra. An electron injected at energy E can decay nonradiatively (through interactions with other electrons in the system) to energy E' as depicted in Fig. 4, and *then* decay radiatively generating a photon of energy $\hbar\omega$. There is therefore an inelastic background to the spectrum which can be written in the form

$$N'(\hbar\omega,E)=\int_{E_F+\hbar\omega}^{E} N(\hbar\omega,E')\beta'(E,E')dE' , \tag{11}$$

where $\beta'(E,E')$ is a partial nonradiative decay probability related to the total probability through

$$\beta(E)=\int_{E_F}^{E}\beta'(E,E')dE' . \tag{12}$$

For a true comparison $N'(\hbar\omega,E)$ should be added to the theoretical prediction, or some estimate of it should be removed from the experimental data. Procedures for doing the latter have been described by Dose and Reusing.[12] In this paper we shall do neither. Because of the various approximations which go into the theory, we regard it as adequate at our present level to compare the untreated ex-

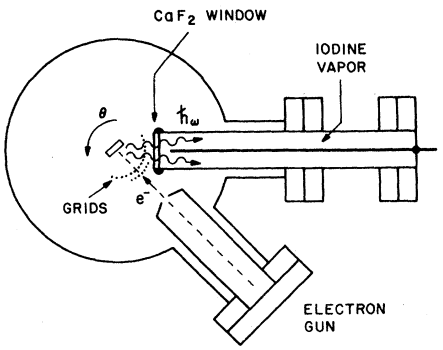

FIG. 5. Experimental configuration. The Geiger-Müller photon detector is oriented with its axis 45° to the incoming electron beam. The angle of incidence θ is varied by rotating the sample.

perimental data with the elastic direct contribution represented by Eq. (1). The function $\beta'(E,E')$ is, of course, closely related to the electron-energy-loss function. Consequently we might expect sharp peaks in $N(\hbar\omega,E)$ to have satellites associated with the plasmon peaks and other structures in $\beta'(E,E')$.

Another omission is the neglect of photon polarization considerations. The $|P_{fi}|^2$ factor in the integrand of Eq. (1) should really be $|\vec{P}_{fi}\cdot\vec{A}|^2$ where $\vec{A}$ is the vector potential associated with the emitted electromagnetic-radiation field. The set of polarization selection rules familiar in angle-resolved photoemission studies would then come into play. We justify our present neglect of these factors on the grounds that: (a) our apparatus does not distinguish photon polarization, and (b) we collect photons over such a large solid angle that polarization effects are largely averaged away.

III. EXPERIMENTAL METHOD

Our experimental KRIPES apparatus is similiar to that of Denninger *et al.*[13] The photon detector is an iodine-filled Geiger-Müller counter with a CaF_2 window. This serves as a band-pass detector with full width at half maximum (FWHM) ~ 0.7 eV centered on the photon energy 9.7 eV. The geometrical arrangement of sample, detector, and electron source is shown schematically in Fig. 5. The detector accepts about 10% of the total 2π steradians of emitted flux. The angle of incidence θ of the incoming electrons is varied by rotating the sample. Since the detector remains fixed, this procedure also varies the angles of photon collection relative to the crystal axes. It is believed, however, that the basic phenomena should not depend critically on photon direction.[3] We are in any case integrating over photon polarization and over a large range of photon collection angles.

The feature which distinguishes our experiments from earlier work is the directional nature of the electron source. It is this that permits us to vary θ in a systematic fashion. We have used a commercial electron gun operating at 40 eV. To decelerate the electrons to the desired incident energies ($\sim 4-14$ eV) we operated in either of two modes: (a) The decelerating potentials were applied across a pair of parallel grids interposed between sample and source, as indicated in Fig. 5; (b) The decelerating potentials were applied directly to the sample with the grids removed. Mode (a) is clearly more satisfactory since the electrons approach the sample in a field-free region, and the measured values of θ are not susceptible to perturbation by irregularities in the equipotential surfaces around the sample as in mode (b). Mode (a), however, did suffer from the disadvantage that bremsstrahlung generated by 40-eV electrons striking the first grid were able to reach the detector and give rise to a large uniform background to the measured spectra. Much of the exploratory work was therefore done in mode (b). Mode (b) was found to be completely satisfactory in the case of normal incidence of the electrons. In future design modifications, it would obviously be desirable to position the decelerating grids out of line of sight of the photon detector.

The Geiger-Müller counter was fabricated from a 25-mm-diameter stainless-steel tube and standard Conflat-flange vacuum hardware. The CaF_2 window was sealed to one end of the tube using ultrahigh-vacuum-compatible epoxy cement. The central electrode was made by extension of a standard medium-high-voltage feedthrough. Room-temperature saturation vapor pressure of iodine ($\lesssim 1$ Torr) was maintained by leaving open a valve to a stainless-steel side tube containing a few crystals of iodine. This valve was closed during bake-out. An unexpected finding was that optimum

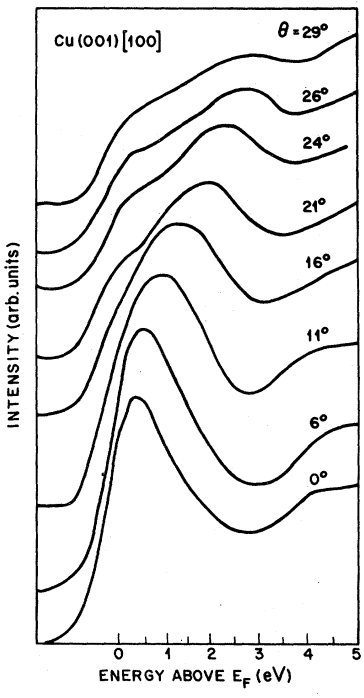

FIG. 6. Variation of the $\hbar\omega=9.7$ eV isochromat spectra from Cu(001) as a function of angle of electron incidence θ. Energies are in eV referred to the Fermi edge.

operation of this remarkably simple detector was obtained *without* presence of the He or other buffer gas normally used in such devices.[13,14] The operating voltage was ~ 340 V. This arrangement presumably leads to much lower gain in the pulse amplification than is usual in Geiger-Müller tubes, but the pulses were readily detected by a data acquisition system used previouly for angle-resolved photoemission work and designed to handle the typical output of a channel-electron multiplier. Counting rates were several hundred per second for typical incident electron currents of $\sim 6\ \mu$A. A spectrum over a 10-eV range with reasonably good statistics could be acquired in $\sim 0.5-1$ hr.

The samples were prepared by the usual cycles of Ar-ion bombardment and annealing. The base pressure of the ultrahigh vacuum system was $\sim 2\times 10^{-10}$ Torr.

IV. RESULTS AND DISCUSSION

A. Cu(001)

Our most important new result is the observation of energy dispersion of peaks in the KRIPES data. This is illustrated in Fig. 6 which shows spectra taken on Cu(001) as a function of angle of incidence θ. At normal incidence a prominent peak is seen just above the Fermi edge. On increasing θ, the peak moves to progressively higher energies and decreases in prominence.

As discussed in Sec. II B, a peak is expected for normal incidence on Cu(001) at 0.4 eV above E_F due to a direct transition between bands 7 and 6. The theoretically predicted dispersion for this feature on increasing θ (or equivalently $\vec{k}_{||}$) is compared with experiment in Fig. 7. Results were obtained in both of the high-symmetry azimuths. The agreement between the theoretical and experimental $E_f(\vec{k}_{||})$ dispersion curves is very good. It is, however, necessary to distinguish which of the various branches (a, b, or c) the experimental data is expected to follow. To distinguish between branches a and b and branches a and b' we examine the electron wave functions of the corresponding initial states, looking for a strong component of the plane wave $\exp[i(\vec{k}+\vec{G}_{00\bar{2}})\cdot\vec{r}]$ since this is the wave which can match most effectively to the incoming electron beam. We propose to write the coupling probability

$$c_i = |u_i(\vec{k}+\vec{G}_{00\bar{2}})|^2 , \tag{13}$$

where $u_i(\vec{k}+\vec{G}_{00\bar{2}})$ is the component of this particular wave in the eigenvector associated with the eigenvalue $E_i(\vec{k})$. The variation of c_i with $\vec{k}_{||}$ is shown for branches a, b, and b' in Fig. 7. (The values of u_i for branch c are identically zero, so this branch can be eliminated from consideration.) The high values of c_i are associated with branch a at low $\vec{k}_{||}$ and, after crossing a gap, with branches b or b' at higher $\vec{k}_{||}$. The experimental points follow the high c_i character. Our present resolution is too poor to actually detect the gaps between branch a and branches b or b'.

The dispersion behavior described above is the same in its essentials as that predicted by the simpler and more physically transparent two-band approximation expounded in Sec. II C. The $E_f(\vec{k}_{||})$ dispersion relation of Eq. (7) is drawn as the dashed curve in Fig. 7. (It has been moved on

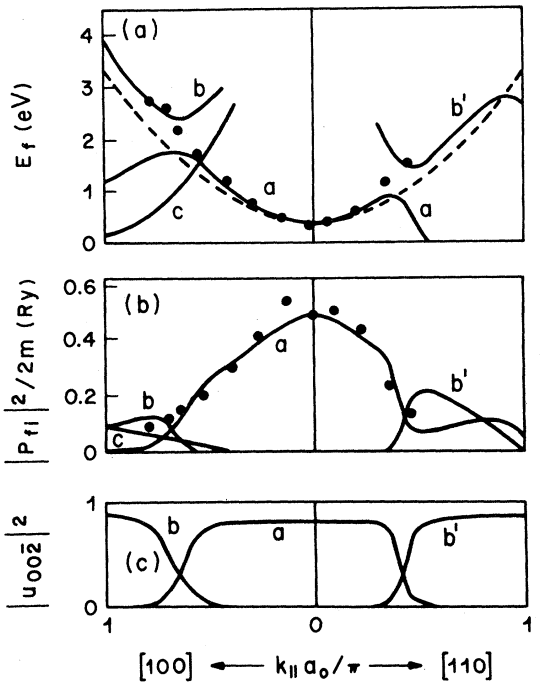

FIG. 7. Theory and experiment for Cu(001) for $\vec{k}_{||}$ along the two principal azimuths [100] and [110]; (a) the experimental energy dispersion results (full circles) are compared with the theoretical $E(\vec{k}_{||})$ relations for bulk direct transitions (full curves); the dashed curve represents the two-band approximation; (b) experimental peak intensities (full circles) are compared with calculated momentum matrix elements; (c) variation of the penetration probability (identified with $|u_i(\vec{k}+G_{00\bar{2}})|^2$) showing how the high-penetration probability is transferred from branch a to branches b or b' with increasing $\vec{k}_{||}$. a_0 is the bulk-lattice parameter ($=3.615$ Å for Cu).

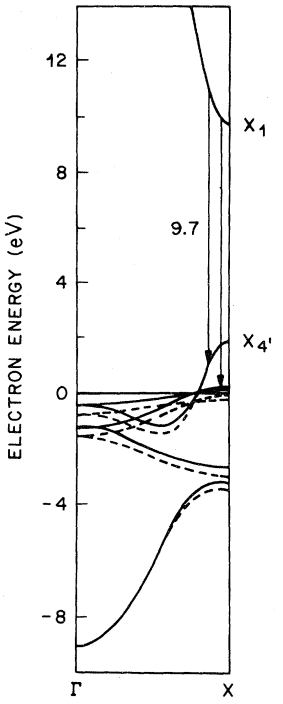

FIG. 8. Band structure of Ni along the ΓX direction, appropriate to normal electron incidence on Ni(001). Vertical arrows indicate the possible direct transitions at $\hbar\omega=9.7$ eV. Dashed curves distinguish the majority from the minority-spin band structure.

the vertical scale so as to match the full curve at $\vec{k}_{||}=0$.) Within the limits of experimental resolution, the experimental dispersion agrees almost as well with the two-band prediction as the full band-structure prediction.

The intensity variations with θ are also well explained by the band-structure model. The calculated momentum matrix elements are compared with experimental peak intensities in Fig. 7. Experiment has been normalized to theory at $\vec{k}_{||}=0$. The experimental points were obtained rather crudely by sketching in an estimate of the inelastic background. The quantitative details of this intensity comparison should therefore not be taken too seriously. The main point is that the decline in magnitude of the observed peak with increasing $\vec{k}_{||}$ is expected. Note that the two-band approximation would be inadequate here since according to Eq. (10) it predicts constant momentum matrix elements.

B. Ni(001)

A principal difference between Ni and Cu is that in Ni the d band is partially unoccupied and should therefore be visible in IPES. The ferromagnetic band structure of Ni along ΓX [appropriate to normal incidence KRIPES on Ni(001)] is shown in Fig. 8. Two direct transitions are possible at $\hbar\omega=9.7$ eV. Firstly, just as in Cu(001), a transition is possible between the sp-like bands $7\rightarrow 6$ depositing an electron at 1.2 eV above E_F. Secondly, there are direct transitions energetically possible into the unoccupied parts of the minority-spin d bands. One of these ($\Delta_1\rightarrow\Delta_2$) is symmetry forbidden, but the other ($\Delta_1\rightarrow\Delta_5$) is permitted. The $\Delta_1\rightarrow\Delta_5$ transition deposits an electron at 0.1 eV above E_F.

KRIPES data for Ni(001) as a function of θ are shown in Fig. 9. There are two main features. Just above E_F we see a shoulder which we attribute to transitions into the minority-spin d band. The second feature is a peak which occurs at 1.2 eV above E_F for $\theta=0°$ and then disperses to higher energies with increasing θ. This second peak is attributed to the expected transition between the sp-like bands $7\rightarrow 6$. The theoretical and experimental $E(k_{||})$ dispersion relations for this particular transition are compared in Fig. 10. The agreement is seen to be quite good. We show (dashed curve) the

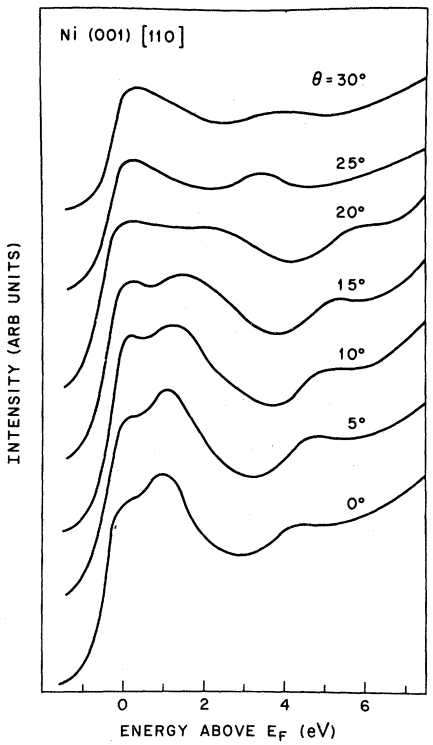

FIG. 9. Variation of the $\hbar\omega=9.7$ eV isochromat spectra from Ni(001) as a function of the angle of electron incidence θ. Energies are in eV referred to the Fermi edge.

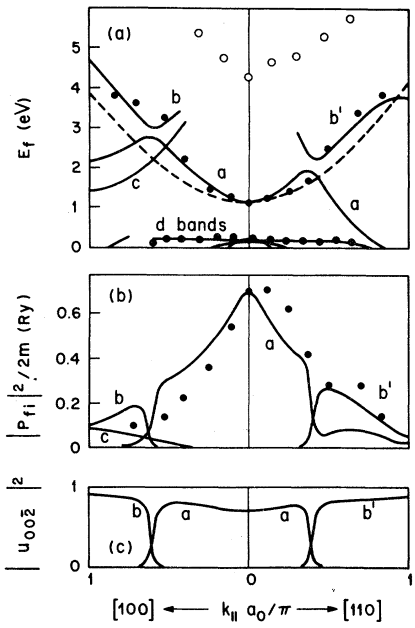

FIG. 10. Theory and experiment for Ni(001) for the two principal azimuths [100] and [110]; (a) the experimental energy dispersion results (full circles) are compared with the theoretical $E(\vec{k}_{\parallel})$ relations for bulk direct transitions (full curves); the dashed curve represents the two-band approximation; (b) experimental peak intensities (full circles) are compared with calculated momentum matrix elements; (c) variation of the penetration probability (identified with $|u_i(\vec{k}+\vec{G}_{00\bar{2}})|^2$) showing how the high-penetration probability is transferred from branch a to branches b or b' with increasing $\vec{k}_{\parallel}$. a_0 is the bulk-lattice parameter ($=3.524$ Å for Ni).

prediction of the two-band model which within the limits of experimental resolution, also agrees with the data. Figure 10 also shows a comparison between the calculated momentum matrix elements and the experimental peak intensities. The experimental intensities were again obtained by using a crudely estimated linear background. The closeness of the quantitative agreement should not be taken too seriously. As in the case of Cu(001), we would merely observe that in both theory and experiment the intensity is maximum at $\vec{k}_{\parallel}=0$ and then decreases with $\vec{k}_{\parallel}$, with the intensity dropping to half its maximum value at $\vec{k}_{\parallel}\sim(0.2-0.3)\pi/a_0$.

We show in Fig. 10 the experimental dispersion relation (open circles) of a weak feature seen in the experimental spectra of Fig. 9. Repeated cycles of argon bombardment and annealing show that this is a persistent feature of the clean Ni(001) surface. It falls in an absolute gap of the bulk band to structure, and is possibly a surface state or surface-barrier resonance. We cannot completely exclude the possibility that it is an adsorbate state due to residual contamination. It may also be an energy-loss satellite. These matters remain under investigation and will be reported elsewhere.[15] A similar feature can be discerned in the spectra for Cu(001) shown in Fig. 6.

Let us consider now the relative intensity of transitions into the sp band and into the d band. For the case of normal incidence this means transitions from band 7 (Δ_1 symmetry) into band 6 (Δ_1 symmetry) and into band 5 (Δ_5 symmetry). The comparison between theory and experiment is made in Fig. 11. The theoretical histograms were obtained by performing the integral of Eq. (1) over the volume Ω comprising a thin rod of square cross section oriented along the ΓX direction and having a width $\Delta\vec{k}_{\parallel}=0.08(\Gamma X)$, corresponding to an angular resolution of $\sim 5°$. Excursions away from $\vec{k}_{\parallel}=0$ have the effect of lowering the symmetry selection rules and thus permitting transitions into the d bands which would not occur had we adhered strictly to $\vec{k}_{\parallel}=0$. Nevertheless, it is

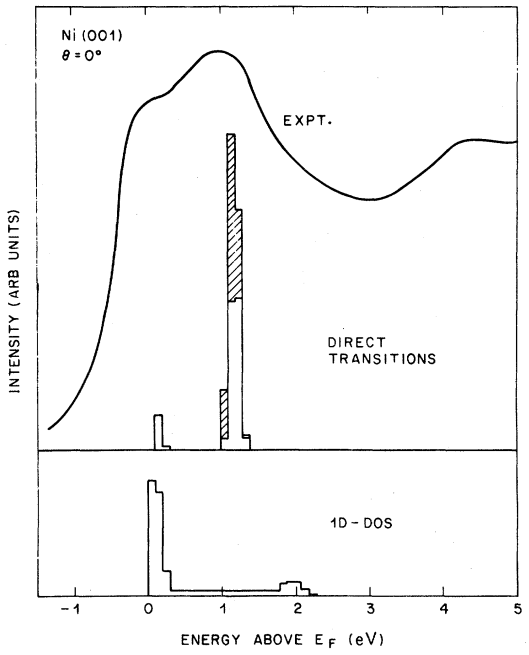

FIG. 11. Normal incidence KRIPES on Ni(001): Experimental and theory showing the relative intensities of emission into the s, p, and d bands. The full curve representing experimental data is compared with a histogram representing the direct-transition prediction including momentum matrix elements $|P_{fi}|^2$ and penetration probability c_i; cross-hatching distinguishes majority from minority-spin contributions. The lower histogram is the total one-dimensional density of states along ΓX.

seen that transitions into the *sp* band are predicted to be much more intense than into the *d* bands—in agreement with the experimental observations. For a closer comparison between theory and experiment, we should convolute the theoretical histograms with an instrumental—resolution and lifetime—broadening function and add an inelastic background as discussed in Sec. II E.

At the DOS level of interpretation in which $\vec{k}_\perp$ conservation is relaxed and both c_i and $|P_{fi}|^2$ are treated as constants, the spectra are expected to resemble the 1D DOS. Calculations of the 1D DOS performed over the same rod in $\vec{k}$ space are shown in Fig. 11. The 1D DOS has an intense minority *d*-band peak just above E_F, and a much weaker *s*,*p* feature at 2.0 eV above E_F. In the case of normal emission from Ni(001), the direct transition model is superior to the 1D DOS comparison both in terms of energy positions of the observed peaks and qualitative features of the relative intensities.

C. Ni angle integrated

The absence of a prominent *d*-band peak in the Ni(001) KRIPES data was initially surprising since it appeared to conflict with previously published data on Ni by Dose *et al.*[16] which showed a prominent *d*-band feature. We sought an answer to this apparent discrepancy in the different experimental configurations. The electron source in the apparatus used in Ref. 16 is a filament very close to the sample. The range of angles of electron incidence is quite wide ($\sim 70°$) so that the data may be regarded as extensively angle integrated. In other words, the results may be simulated by taking the volume of integration Ω in Eq. (1) to be the entire Brillouin zone. The results of such a calculation are compared with experiment in Fig. 12. The intense peak observed experimentally just above E_F is now apparent in the experimental spectrum. We identify the peak at 1.5 eV above E_F in the experimental spectrum with the square-topped feature in the theoretical histogram centered at the same energy. The theoretical peak at 2.8 eV appears to be associated with the rather weak peak at 3.1 eV in the experimental data.

Also shown in Fig. 12 is the total DOS. This would correspond to complete relaxation of $\vec{k}$ conservation and the treatment of c_i and $|P_{fi}|^2$ as constants. The DOS displays a very intense peak due to the unoccupied minority *d*-band states just above E_F, but fails to show any features at higher

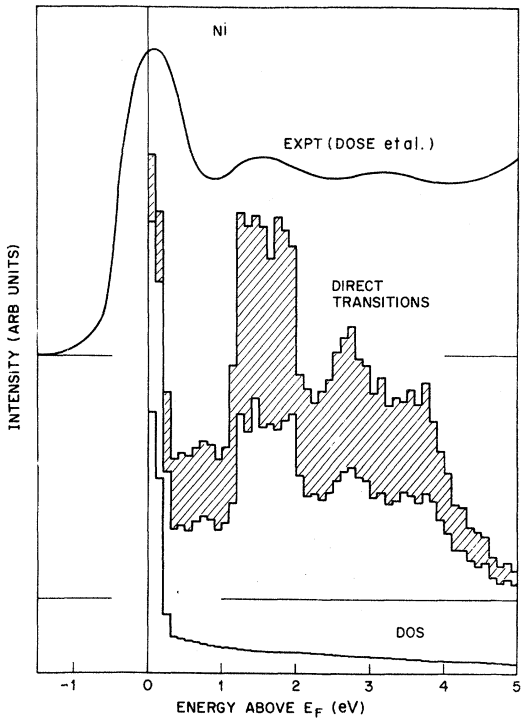

FIG. 12. IPES (angle-integrated) data of Ref. 16 represented by the full curve is compared with two theoretical models. The upper histograms represent the predictions of the direct-transition model with full inclusion of momentum matrix elements; integration has been performed over the entire Brillouin zone; cross hatching distinguishes the majority from the minority-spin contribution. The lowest histogram is the total unoccupied density of states.

energies. In terms of energy locations, the direct-transition model is quite successful, where as a simple DOS model is incomplete.

In terms of relative intensities, a proper comparison with experiment would require convolution of the theoretical spectrum with the instrumental resolution function and the addition of an inelastic background as discussed in Sec. II E. This has not been done, but we can predict that because of its inherently narrow width, the *d* peak will be very much reduced in relative prominence. It may therefore be necessary to invoke some additional mechanism for *d* intensity, e.g., transitions involving evanescent initial-state wave functions.[17] On the other hand, the discrepancy may lie in artifacts of the second-principles theoretical approach. Previous experience with the combined interpolation scheme[8] shows that it has a tendency to overestimate the strength ($|P_{fi}|^2$) of optical transitions within the *s*,*p* manifold relative to those between *d* and *s*,*p* states.

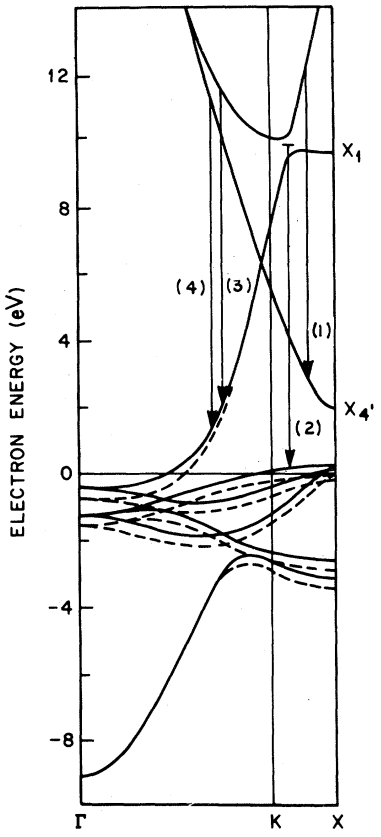

FIG. 13. Band structure of Ni along the ΓKX direction, appropriate to normal electron incidence on Ni(110). Vertical arrows labeled (1)—(4) indicate the possible direct transitions at $\hbar\omega = 9.7$ eV. Dashed curves distinguish the majority from the minority-spin band structure.

D. Ni(110)

Our results on Ni(110) are much less extensive than on Ni(001), and we have confined our attention largely to normal incidence. In this case we are confined to the band structure along the ΓKX line shown in Fig. 13. A number of vertical transitions are possible at $\hbar\omega = 9.7$ eV but not all of these are equally efficacious because of differing values of c_i and $|P_{fi}|^2$, as we shall now consider.

Let us first consider the coupling coefficient c_i appropriate to normal incidence on Ni(110). The plane waves propagating normal to (110), and therefore offering good penetration possibilities, are $\exp(i\vec{k}\cdot\vec{r})$ and $\exp[i(\vec{k}+\vec{G}_{\bar{2}20})\cdot\vec{r}]$. The latter corresponds to higher energies and is not well represented in the range of interest. The wave $\exp(i\vec{k}\cdot\vec{r})$ is well represented. We therefore write

$$c_i = |u_i(\vec{k})|^2 . \tag{14}$$

This has the effect of selecting out those transitions labeled in Fig. 13 as (1) and (2), and suppressing those labeled (3) and (4). [By accident at $\hbar\omega = 9.7$ eV, transition (2) has an initial state in a gap. This does not present a problem since the volume Ω of integration in k space Ω in the calculations presented below is a rod with finite dimensions in $\vec{k}_{||}$. These direct transitions into the d band are able to assert themselves.]

The theoretical calculations for Ni(110) are compared with experiment in Fig. 14. The most intense peak predicted by the direct transition theory occurs at 2.9 eV and is associated with transition (1) of Fig. 13. The experimental spectrum, however, shows no indication of such a peak and displays only one prominent feature just above E_F which is readily associated with the d band. The situation is therefore in marked contrast to the normal incidence data for Ni(001) shown in Fig. 11. In comparing Figs. 11 and 14, however, note that the

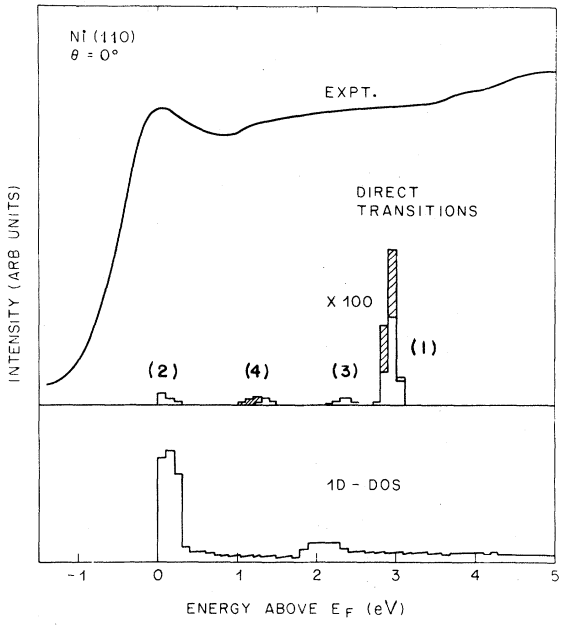

FIG. 14. Normal incidence KRIPES on Ni(110): Experiment and theory showing the relative intensities of emission into the s, p, and d bands. The full curve representing the experimental data is compared with a histogram representing the direct transition prediction including momentum matrix elements $|P_{fi}|^2$ and penetration probability c_i; cross hatching distinguished majority from minority-spin contributions. The lower histogram is the total one-dimensional density of states along ΓKX.

(arbitrary) vertical scales for the theory are the same. It is seen that the predicted intensity of emission associated with bulk direct transitions is more than 2 orders of magnitude smaller on Ni(110) than on Ni(001). Because of this inherent weakness in intensity, the bulk direct-transition model has in a sense disqualified itself for Ni(110). We seek interpretations therefore in terms of other mechanisms such as those involving evanescent initial states and/or abandonment of $k_\perp$ conservation in which the spectrum should resemble the 1D DOS. Calculations of the 1D DOS shown in Fig. 14, indeed show an intense d peak just above E_F, but otherwise only a relatively weak feature at 2.1 eV.

V. SUMMARY AND FORECAST

The results of this investigation may be summarized as follows: (1) We have demonstrated KRIPES and its usefulness; (2) $E(\vec{k}_{||})$ dispersion relations have been observed for Cu(001) and Ni(001); (3) the observed $E(\vec{k}_{||})$ dispersion relation has been successfully interpreted in terms of direct transitions within the bulk band structure; (4) intensity variations with angle of the sp peaks in Cu(001) and Ni(001) correlate well with calculated values for the momentum matrix elements $|P_{fi}|^2$; (5) relative intensities of the sp peak and the minority d-band feature in Ni(001) are qualitatively explained by the calculated $|P_{fi}|^2$; (6) experimental results on Ni(110) are not completely understood in terms of bulk direct transitions and appear to require consideration of density-of-states effects.

Where does the KRIPES technique go from here? Even with the present constraints of fixed photon energy (9.7 eV) and rather poor resolution ($\sim$0.7 eV), the technique is quite useful. We anticipate studies of the empty states of metals and semiconductors in the energy range between E_F and the vacuum level, a region inaccessible in ordinary PES. These studies will investigate both bulk states, surface states, and adsorbate-induced states. It is of interest to speculate on how such investigations will stimulate, and will in turn be driven by improvements in experimental technique.

It would be very desirable to be able to vary $\hbar\omega$. One can envisage working with a set of different band-pass filter detectors.[14,18] The upper limit of such devices is determined by the transmission cutoff of LiF ($\hbar\omega \sim 11.7$ eV) and the energy resolution is not particularly good. Ultimately, we must contemplate some sort of grating spectrograph.[19] To attain acceptable energy resolution, the angular acceptance aperture of the grating must be considerably smaller than that possible with band-pass filter detectors. To compensate for this, some sort of multidetection is required.[20] Parallel detection in $\hbar\omega$ corresponds to the so-called CIS (constant initial state) mode in ordinary PES. The isochromat mode corresponds to the EDC (energy-distribution curve) mode.

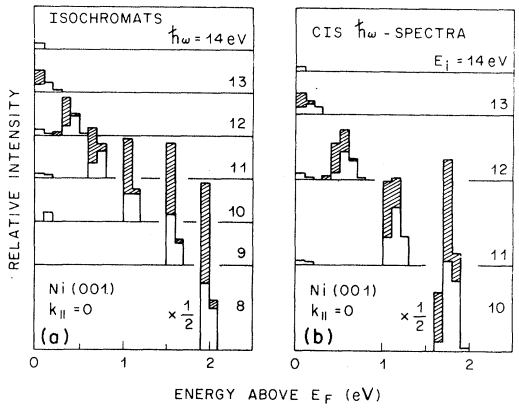

FIG. 15. Theoretical predictions for normal incidence KRIPES on Ni(001): (a) isochromats (or EDC's) for photon energies in the range $\hbar\omega = 8-14$ eV; (b) photon energy scans (or CIS's) for various incident electron energies E_i. Cross hatching distinguishes the majority-spin contribution. The spectra are plotted against final energies E_f referred to the Fermi level E_F.

In anticipation of such experimental developments, we present some theoretical predictions of what one might expect to observe on the basis of the bulk-band-structure direct-transition model for the particular case of normal incidence KRIPES on Ni(001). Figure 15 compares the calculated spectra for the EDC and CIS modes. The volume of $\vec{k}$-space integration Ω was, as before, a rod centered on ΓX with diameter $\Delta\vec{k}_{||} = 0.08(\Gamma X)$. Figure 15(a) displays the EDC's (isochromats) for a set of discrete energies $\hbar\omega = 8-14$ eV. One sees the d peak just above E_F and the dispersion of the s,p feature. Figure 15(b) displays the CIS's for a number of discrete initial electron energies E_i. Once again we see the d peak and the dispersion of the s,p peak. The peaks are significantly wider, but this should not be construed as an inherent inferiority of the CIS mode. It is simply a joint-density-of-states effect. Since E_f disperses downward into the zone and E_i disperses upward at a similar rate, a change ΔE_f implies a change in

photon energy $\Delta\hbar\omega \sim 2\Delta E_f$. Figures 15(a) and 15(b) carry identical information. The challenging prospect is that CIS spectra can be obtained in parallel detection using the advanced spectrographs which are being developed[19,20] as the next generation of IPES instrumentation.

---

*Permanent address: Dept. of Physics, University of Warwick, Coventry CV4 7AL, United Kingdom.

[1]For reviews see K. Ulmer, in *Band Structure Spectroscopy of Metals and Alloys,* edited by D. J. Fabian and L. M. Watson (Academic, London, 1973), p. 521; D. J. Nagel, *ibid.,* p. 457.

[2]V. Dose, Appl. Phys. 14, 117 (1977).

[3]J. B. Pendry, J. Phys. C 14, 1381 (1981); Phys. Rev. Lett. 45, 1356 (1980).

[4]A preliminary announcement of this work has been made by D. P. Woodruff and N. V. Smith, Phys. Rev. Lett. 48, 283 (1982); N. V. Smith and D. P. Woodruff, Phys. Rev. B 25, 3400 (1982).

[5]A similar theoretical approach is presented in outline by P. O. Nilsson and C. G. Larsson, Jpn. J. Appl. Phys. 17, Suppl. 17-2, 144 (1978).

[6]A Liebsch, Phys. Rev. B 13, 544 (1976); J. B. Pendry, Surf. Sci. 57, 679 (1976); B. Holland, *ibid.* 68, 490 (1977).

[7]See *Photoemission in Solids I,* Vol. 26 of *Topics in Applied Physics,* edited by M. Cardona and L. Ley (Springer, Berlin, 1978); C. N. Berglund and W. E. Spicer, Phys. Rev. 136, A1030 (1964); 136, A1044 (1964).

[8]N. V. Smith, Phys. Rev. B 19, 5019 (1979). The parameters of the interpolation scheme for Cu are taken from R. Lässer, N. V. Smith, and R. L. Benbow, Phys. Rev. B 24, 1895 (1981). Those for Ni are from N. V. Smith, R. Lässer, and S. Chiang, *ibid.* 25, 793 (1982). Spin-orbit splitting is neglected in both cases.

[9]N. V. Smith and W. E. Spicer, Phys. Rev. 188, 593 (1969); R. Y. Koyama and N. V. Smith, Phys. Rev. B 2, 3049 (1970); T. Gustafsson, P. O. Nilsson, and L. Wallden, Phys. Lett. 37A, 121 (1971); H. Y. Fan, Phys. Rev. 68, 43 (1945).

[10]G. D. Mahan, Phys. Rev. B 2, 4334 (1970).

[11]See *Photoemission and the Electronic Properties of Surfaces,* edited by B. Feuerbacher, B. Fitton, and R. F. Willis (Wiley, New York, 1978).

[12]V. Dose and G. Reusing, Appl. Phys. 23, 131 (1980).

[13]G. Denninger, V. Dose, and H. Scheidt, Appl. Phys. 18, 375 (1979).

[14]J. A. R. Samson, *Techniques of Vacuum Ultraviolet Spectroscopy* (Wiley, New York, 1967), p. 251.

[15]P. D. Johnson and N. V. Smith (unpublished).

[16]V. Dose, Th. Fauster, and H. Scheidt, J. Phys. F 11, 1801 (1981).

[17]G. Denninger, V. Dose, and H. P. Bonzel, Phys. Rev. Lett. 48, 279 (1982); G. Denninger, V. Dose, M. Glöbl, and H. Scheidt, Solid State Commun. 42, 583 (1982).

[18]A. Kovacs, P. O. Nilsson, and J. Kanski, Phys. Scr. 25, 791 (1982).

[19]G. Chauvet and R. Baptist, J. Electron. Spectrosc. 24, 255 (1981).

[20]Progress has already been made by F. J. Himpsel and Th. Fauster (unpublished).